RSC Advances

PAPER

View Article Online
View Journal | View Issue



Cite this: *RSC Adv.*, 2023, **13**, 5197

# Piperonal chalcone derivative incorporating the pyrazolo[3,4-*b*]pyridine moiety; crystal structure, spectroscopic characterization and quantum chemical investigations†

Efraín Polo-Cuadrado,[a] Karoll Ferrer,*[b] Edison Osorio,[c] Iván Brito,[d] Jonathan Cisterna,[e] Luis Espinoza,[f] Joel B. Alderete*[g] and Margarita Gutiérrez*[a]

Received 19th December 2022
Accepted 26th January 2023

DOI: 10.1039/d2ra08101f

rsc.li/rsc-advances

A single crystal of a piperonal chalcone derivative was obtained, fully characterized, and crystallized by a slow evaporation technique. The synthesized compound was characterized by UV-Visible, FT-IR, HRMS, $^{1}$H NMR, and $^{13}$C NMR spectroscopic studies and X-ray crystallography, revealing that the crystal belongs to a triclinic crystal system with a $P\bar{1}$ space group, $Z = 2$. In the present work, we focus on molecular modeling studies such as Hirshfeld surface analysis, energy framework calculations, frontier molecular orbital analysis, natural bond orbital analysis, and NLO properties of a π-conjugate system combining the chalcone and the pyrazole[3,4-*b*]pyridine scaffolds to describe the in-depth structural analysis thereof. Good agreement was found between the calculated results and experimental data. In addition, Hirshfeld surface analysis of the crystal structure showed that the intermolecular stabilization in the crystal packing comes mainly from H···H bond interactions. The chalcone crystal exhibits significant NLO properties suggesting that it could be considered a potential candidate for application in nonlinear optical devices.



## 1 Introduction

Nonlinear optical (NLO) materials possess optical properties that depend on the intensity of incident light.[1] NLO materials significantly impact different fields, such as medicine and photonics. Additionally, they are widely used in industrial applications such as second harmonic generation (SHG), optical modulation, optical switching, laser technology, optical data storage, electro-optical switches, optical logic, signal processing, ultra-fast optical communication, and for optical limiting purposes.[2–8]

The NLO properties of a material depend on the degree of charge separation (molecular hyperpolarizability) induced by light and the photoinductive changes of the molecular dipole moment.[1,9] Thus, in general, the NLO properties of inorganic substances depend on their constituent ions. In contrast, the NLO properties of organic substances depend on the intermolecular donor–acceptor interaction, delocalized π electron systems, and their ability to crystallize non-symmetrically to the center.[8] Current research trends have been focused on organic materials, mainly those with chromophore groups and widely delocalized π electron structures, since their NLO coefficients are higher than those of inorganic materials.

From the perspective of optical device applications, organic materials could be considered the "materials of the future" due to unique properties such as ultra-fast optical response, high resistance to damage, broader transparency down to the blue region, ease, and low cost of production. Furthermore, their architectural flexibility allows modification at the molecular level of these compounds, which is suitable for obtaining large crystals of high optical quality and desired optical properties.[8,10] Molecular improvements such as increased planar conformations and chromophore groups in organic structures have attracted attention, as they have been reported to enhance NLO

[a]*Laboratorio Síntesis Orgánica y Actividad Biológica (LSO-Act-Bio), Instituto de Química de Recursos Naturales, Universidad de Talca, Casilla 747, Talca 3460000, Chile. E-mail: mgutierrez@utalca.cl*

[b]*Laboratory of Growth Regulators, Institute of Experimental Botany, The Czech Academy of Sciences, Palacký University, Šlechtitelů 27, 78371 Olomouc, Czech Republic. E-mail: karoll.ferrerpertuz@upol.cz*

[c]*Facultad de Ciencias Naturales y Matemáticas, Universidad de Ibagué, Carrera 22 Calle 67, Ibagué 730001, Colombia*

[d]*Departamento de Química, Facultad de Ciencias Básicas, Universidad de Antofagasta, Campus Coloso, Antofagasta 02800, Chile*

[e]*Departamento de Química, Facultad de Ciencias, Universidad Católica del Norte, Sede Casa Central, Av. Angamos 0610, Antofagasta, Chile*

[f]*Departamento de Química, Universidad Técnica Federico Santa María, Av. España No. 1680, Valparaíso 2340000, Chile*

[g]*Instituto de Química de Recursos Naturales (IQRN), Universidad de Talca, Avenida Lircay S/N, Casilla 747, Talca, Chile. E-mail: joel.alderete@utalca.cl*

† Electronic supplementary information (ESI) available. CCDC 2218131. For ESI and crystallographic data in CIF or other electronic format see DOI: https://doi.org/10.1039/d2ra08101f

activity. In this regard, increased planarity contributes to electron mobility within the π-conjugated molecular system, while chromophore groups increase the hyperpolarizability of the molecule.[11,12]

Among the organic compounds, chalcones stand out due to their high tendency to crystallize, resistance to laser damage, excellent second and third-order NLO responses, and extensive applications in biological and pharmaceutical fields.[5,13–15] Several experimental studies have been conducted on the NLO properties of various chalcones, and encouraging results have been reported for future applications such as nonlinear frequency conversion, nonlinear refraction, optical limiters, and SHG (15 times greater than urea).[5,8,16–20]

However, although chalcones are an essential group of molecules in terms of NLO properties, structural building blocks such as pyrazoles and pyridines are relevant groups that confer planarity and extension of the delocalized π-electron conjugation to the systems into which they are incorporated. Specifically, it has been found that the asymmetric electronic distribution can be improved in either or both the ground state and excited state configurations by adding the appropriate functionality at the ends of the conjugated chalcone systems, leading to an increase in NLO. Electron donor and acceptor components result in a considerable change in hyperpolarizability.[9,12,21–24]

Hence, prompted by the above observations and our interest in pyrazolopyridine derivatives, we have focused on the structural properties of a piperonal chalcone derivative incorporating the pyrazolo[3,4-*b*]pyridine moiety. Apart from XRD, UV-Visible, FT-IR, HRMS, and NMR experimental techniques, confirmation of the stable crystal structure has been based on the results of quantum chemistry such as geometry optimization, Hirshfeld surface analysis, energy framework calculations, frontier molecular orbitals (FMOs) analysis, natural bond orbital (NBO) analysis, and nonlinear optical (NLO) properties of the title compound.

# 2 Experimental

## 2.1 Materials and methods

All chemical reagents and organic solvents were obtained from commercial suppliers and used without further purification. The experiments were performed in a Discover microwave apparatus (CEM Corporation, USA) and a Branson 1510 ultrasonic cleaning bath with a mechanical timer and a heater switch, 47 kHz. Thin-layer chromatography (TLC) was performed to check the purity of compounds on silica gel 60 $H_{F254}$ plates (Merck, Germany). The melting point ranges (mp) were taken on an Electrothermal IA9100 apparatus (Stone, UK) using the one-end open capillary method and were uncorrected. IR spectra (KBr discs, 500–4000 $cm^{-1}$) were recorded on a NEXUS 670 FT-IR spectrophotometer (Thermo Nicolet, USA). $^1H$ and $^{13}C$ NMR spectra were recorded using DMSO-$d_6$ and $CDCl_3$ as solvents and tetramethylsilane (TMS) as an internal reference on an AM-400 spectrometer (Bruker, Germany) at working frequencies 400 and 100 MHz, respectively. High-resolution mass spectrometry (HRMS) analyses were carried out using a Bruker "Compact" quadrupole time-of-flight mass spectrometry (qTOF-MS, Germany) coupled with an Apollo II ion funnel electrospray ionization (ESI) source. The UV-Vis spectrum was recorded using a Spectroquant UV/VIS Pharo 300 Spectrophotometer (Merck, Germany) in the wavelength range of 160–750 nm.

## 2.2 Synthesis of 1-(3,6-dimethyl-1-phenyl-1*H*-pyrazolo[3,4-*b*]pyridin-5-il)etanone (4)

Pyrazolo[3,4-*b*]pyridine **4** was synthesized according to our previously reported procedure (Scheme 1).[25] A catalytic amount of $InCl_3$ (15% mol) was added to a solution of equimolar amounts of 5-aminopyrazole **1** (1 mmol), *p*-formaldehyde **2** (1 mmol), and acetylacetone **3** (1 mmol) in water (3 mL). A focused microwave reactor irradiated the mixture at 300 MW and 210 °C for 17 min. The reaction mixture was poured into water and extracted with ethyl acetate (2 × 10 mL). The combined organic layers were dried over $Na_2SO_4$ and concentrated to afford the title compound **4** (238.7 mg, 90% yield) as a yellow solid. mp: 100–102 °C; IR (KBr, $cm^{-1}$): 3065, 2960, 2924, 2853, 1679, 1611, 1592, 1503, 1436, 1236, 1119, 1026, 944, 755, 692, 585; $^1H$ NMR (DMSO-$d_6$, 400 MHz) $\delta_H$: 2.63 (s, 3H, $CH_3$), 2.67 (s, 3H, $CH_3$), 2.77 (s, 3H, $CH_3$), 7.31 (t, $J = 7.4$ Hz, 1H), 7.54 (t, $J = 8.0$ Hz, 2H), 8.25 (d, $J = 7.7$ Hz, 2H), 8.87 (s, 1H); $^{13}C$ NMR (DMSO-$d_6$, 100 MHz) $\delta_C$: 12.2 ($CH_3$), 25.8 ($CH_3$), 29.4 ($CH_3$), 114.4 (C), 120.1 (2 × CH), 125.7 (CH), 127.2 (C) 129.1 (2 × CH), 133.3 (CH), 138.9 (C), 144.3 (C), 149.5 (C), 158.5 (C), 199.6 (C); HRMS (ESI, *m*/*z*): calculated for $C_{16}H_{16}N_3O$ $[M + H]^+$ 266.1293 found 266.2751.

## 2.3 Synthesis and crystallization of (*E*)-3-(benzo[*d*][1,3]dioxol-5-yl)-1-(3,6-dimethyl-1-phenyl-1*H*-pyrazolo[3,4-*b*]pyridin-5-yl)prop-2-en-1-one (6)

Piperonal chalcone derivative **6** was prepared according to our previously reported experimental procedure (Scheme 1).[25] KOH (1 mmol) was added to a solution of pyrazolo[3,4-*b*]pyridine **4** (1

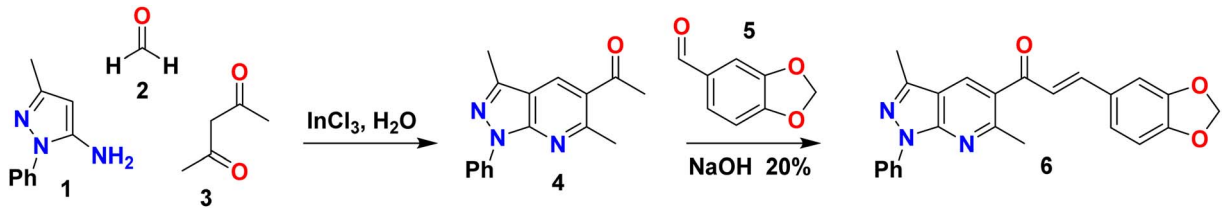


Scheme 1 Synthetic route of (*E*)-3-(benzo[*d*][1,3]dioxol-5-yl)-1-(3,6-dimethyl-1-phenyl-1*H*-pyrazolo[3,4-*b*]pyridin-5-yl)prop-2-en-1-one (**6**).

mmol) and piperonal **5** (1 mmol) in ethanol (2 mL). The mixture was sonicated for 10 min in an ultrasonic cleaning bath. The end of the reaction was detected by TLC using a mixture of solvent (dichloromethane/ethyl acetate 9 : 1) as an eluent. The reaction mixture was allowed to cool down in an ice-cold water bath. A yellow precipitate was collected by vacuum filtration and washed with cold water, followed by recrystallization from ethanol to obtain the desired compound **6** (250.3 mg, 63% yield) as a yellow solid. mp: 186–188 °C; IR (KBr, $cm^{-1}$): 3082, 2990, 2894, 1655, 1589, 1577, 1444, 1308, 1033, 984, 754; $^1$H NMR ($CDCl_3$, 400 MHz) $\delta_H$: 2.63 (s, 3H, $CH_3$), 2.81 (s, 3H, $CH_3$), 6.01 (s, 2H, $CH_2$), 6.82 (d, $J$ = 8.0 Hz, 1H), 7.12–7.04 (m, 3H), 7.28 (t, $J$ = 7.5 Hz, 1H), 7.52–7.45 (m, 3H), 8.16 (s, 1H), 8.32 (d, $J$ = 7.6 Hz, 2H); $^{13}$C NMR ($CDCl_3$, 100 MHz) $\delta_C$: 12.43 ($CH_3$), 24.75 ($CH_3$), 101.64 ($CH_2$), 106.53 (CH), 108.59 (CH), 114.20 (C), 120.60 (2 × CH), 123.97 (CH), 125.34 (CH), 125.57 (CH), 128.72 (C), 128.76 (C), 128.91 (2 × CH), 129.87 (CH), 139.28 (C), 143.36 (C), 145.77 (CH), 148.41 (C), 150.12 (C), 150.16 (C), 158.01 (C), 193.85 (C=O); HRMS (ESI, $m/z$): calculated for $C_{24}H_{20}N_3O_3^+$ $[M + H]^+$ 398.1499, found 398.1499.

### 2.4 X-ray crystal structure determination

Suitable crystals of the piperonal chalcone derivative **6** were chosen for the X-ray crystallographic analysis. X-ray intensity data were collected at 296 K in a Bruker D8 Venture diffractometer equipped with a bidimensional CMOS Photon 100 detector, using Mo-Kα radiation of wavelength 0.71073 Å. The diffraction frames were integrated using the APEX3 package[26] and were corrected for absorption effects using the multi-scan method (SADABS). The crystal structure was solved by intrinsic phasing[27] using the OLEX2 program.[28] Refinement was carried out by full-matrix least-squares methods based on $F^2$ (SHELXL-2014).[27] The figures of the X-ray structure of the title compound were generated with the help of OLEX2 and ORTEP program packages. Crystallographic information files were deposited in the Cambridge Crystallographic Data Centre (CCDC) with the deposition number 2218131.†

## 3 Computational methods

### 3.1 Theoretical calculations

The X-ray diffraction experimental result of the title compound was directly taken for an initial molecular geometry. The geometry optimization of the monomeric structure was carried out using the M062X exchange–correlation functional and 6-311++G(d,p) basis set[29,30] in the gas phase. M062X is a hybrid meta exchange–correlation functional with double the nonlocal exchange (2×), which is parametrized for nonmetal and long noncovalent range interactions.[31] The calculations were performed using Gaussian 09 software.[32]

Optimized structural parameters were used to calculate the $^1$H and $^{13}$C NMR chemical shifts in chloroform with the Gauge-Independent Atomic Orbital (GIAO)[33] method at M062X, TPSS, and B3LYP levels using 311++G(d,p) basis set. The solvent effect on theoretical NMR parameters was included using the Conductor polarizable Continuum Model (CPCM)[34–37] provided by Gaussian 09 program.[32]

The theoretical electronic spectrum of the monomeric structure was performed through the time-dependent density-functional theory (TDDFT) calculations[38,39] at the M062X/6-311++G(d,p) level. The solvent effect of methanol on the calculated electronic properties of the studied compound was investigated using the polarizable continuum model (PCM).[40,41]

The frontier molecular orbitals (FMOs),[42] the highest occupied molecular orbital (HOMO) and lowest unoccupied molecular orbital (LUMO), which account for the ability to donate and accept electrons, were calculated at DFT/M062X/6-311++G(d,p) level. Some global reactivity descriptors, such as HOMO–LUMO gap, chemical hardness ($\eta$), chemical potential ($\mu$), electrophilicity index ($\omega$), and chemical softness ($S$), which are based on the HOMO and LUMO energies were studied to measure the stability of the synthesized molecule.

The natural bond orbital (NBO)[43] calculations of the title compound were achieved at M062X/6-311++G(d,p) level of theory using the NBO 3.1 program within the Gaussian 09 software.[32] Chemcraft program package (**https://www.chemcraftprog.com**) was used to draw the molecular graphs.

### 3.2 Nonlinear optical (NLO) details

The electric dipole moment, linear polarizability, and the first and second hyperpolarizability tensors were evaluated using FF approach to explore the non-lineal optical (NLO) properties of the title compound with a field frequency of 0.0010 au at the DFT/DCAM-B3LYP/6-311G++(d,p) level.

DFT functional has shown results close to CCSD and MP2 methodologies,[44,45] indicating efficiency and accuracy for calculation of second order hyperpolarizability. In the finite field (FF) method, when a molecule is subjected to a static field ($F$), the energy ($E$) of the molecule can be expressed as:

$$E = E^\circ - \mu_i F_i - \frac{1}{2}\alpha_{ij}F_iF_jF_k - \frac{1}{2}\gamma_{ijkl}F_iF_jF_kF_l - \ldots$$

where $E^\circ$ is the energy of the molecule in the absence of an electronic field, $\mu$ is a component of the dipole moment vector, and it is given as:

$$\mu = (\mu_x{}^2 + \mu_y{}^2 + \mu_z{}^2)^{1/2}$$

On the other hand, $\alpha$ corresponds to the linear polarizability tensor, while $\beta$ and $\gamma$ are the first and second hyperpolarizability tensors, with $i, j$, and $k$ as the labels for $x$, $y$, and $z$ components, respectively. The tensors equations are given as follows:

$$\langle\alpha\rangle = \frac{1}{3}(\alpha_{xx} + \alpha_{yy} + \alpha_{zz})$$

$$\langle\beta\rangle = [(\beta_{xxx} + \beta_{xyy} + \beta_{xzz})^2 + (\beta_{yyy} + \beta_{yzz} + \beta_{yxx})^2 + (\beta_{zzz} + \beta_{zxy} + \beta_{zyy})^2]^{1/2}$$

$$\langle\gamma\rangle = \frac{1}{5}\left[\gamma_{xxxx} + \gamma_{yyyy} + \gamma_{zzzz} + 2\left[\gamma_{xxyy} + \gamma_{yyzz} + \gamma_{xxzz}\right]\right]$$

### 3.3 Hirshfeld surface analysis details

Hirshfeld surface analysis and 2D-fingerprint plots[46] were carried out using the CrystalExplorer 21.3 software[47] to determine significant intermolecular interactions and contacts in the crystal structure of the studied compound. For computations, the crystallographic information file (*.cif) was initially used for the analysis. Two distances were calculated for each point on the Hirshfeld isosurface, $d_e$ and $d_i$, representing distances from a point on the surface to the nearest nucleus outside and inside the surface. All measures were normalized using $d_{norm}$ distance (normalized contact distance), which is defined in eqn (1) and is based on $d_e$, $d_i$ and the van der Waals radius (vdW) for $d_e$ and $d_i$ atoms within the compound.[48,49]

$$d_{norm} = \frac{d_i + r_i^{vdW}}{r_i^{vdW}} + \frac{d_e + r_e^{vdW}}{r_e^{vdW}} \quad (1)$$

The electrostatic potentials were mapped on the Hirshfeld surface at B3LYP/6-31G(d,p) level of theory over a range of ±0.002 au.[50] The bond lengths of hydrogen atoms involved in interactions were normalized to standard values from neutron diffraction measurements (C–H = 1.083 Å, N–H = 1.009 Å, O–H = 0.983 Å)[51] for the generation of fingerprint plots. The intermolecular energies of the molecular pairs in the crystal packing were calculated at B3LYP/6-31G(d,p) level of theory in a cluster of radius 3.8 Å around the molecule.[52,53]

## 4 Results and discussion

### 4.1 Chemistry and characterization

Piperonal chalcone derivative **6** was synthesized according to our previously reported experimental procedure outlined in Scheme 1.[25] The one-pot condensation of 5-amino-3-methyl-1-phenylpyrazole **1**, *p*-formaldehyde **2** and β-diketone **3** under microwave irradiation in aqueous media and catalyzed by $InCl_3$ generated the pyrazolo[3,4-*b*]pyridine derivative **4** (90% yield) followed by treatment with piperonal **5** to give the title compound **6** (63% yield). The structure of the piperonal chalcone derivative **6** was characterized by $^1$H NMR, $^{13}$C NMR, FT-IR and HRMS. The $^1$H- and $^{13}$C-NMR assignments have been completed by 1D and 2D heteronuclear correlation HSQC and HMBC techniques.

The $^1$H NMR spectrum of compound **6** was measured in deuterated chloroform and revealed the presence of nineteen protons (see Fig. S1 and Table S1†). The two singlets due to methyl groups linked to the pyrazole and pyridine rings were observed at $\delta_H$ = 2.63 ppm (s, 3H, $CH_3$-6) and $\delta_H$ = 2.81 ppm (s, 3H, $CH_3$-17), respectively. The methylene protons were found at $\delta_H$ = 6.01 ppm (s, 2H, $CH_2$). At the same time, the doublet corresponding to H-24 was shown at $\delta_H$ = 6.82 (d, $J$ = 8.0 Hz, 1H). The presence of signals at $\delta_H$ = 8.32 ppm (d, $J$ = 7.6 Hz, 2H, H-12 and H-16), 7.52–7.45 (m, 2H, H-13 and H-15) and 7.28 (t, $J$ = 7.5 Hz, 1H, H-14) were assigned to aromatic protons of the phenyl group attached to the pyrazolo[3,4-*b*]pyridine system. A singlet observed at $\delta_H$ = 8.16 ppm (s, 1H) was due to the resonance of the pyridine ring proton corresponding to H-11.

The $^{13}$C NMR spectrum of the title compound was measured in deuterated chloroform and revealed the presence of twenty-four carbon atoms consistent with the target compound (see Fig. S2 and Table S1†). $^{13}$C NMR showed a signal at $\delta_C$ = 193.85 ppm assigned to the carbonyl carbon of chalcone, and the signals at $\delta_C$ = 12.43 and 24.75 ppm were attributed to methyl groups $CH_3$-6 and $CH_3$-17, respectively.

Additional evidence for the structure of piperonal chalcone derivative (**6**) was provided from 2D HMBC spectrum, which showed significantly correlated couplings of the α,β-unsaturated ketone system (see Fig. 1). The α-H (H-18) showed correlations with carbonyl group ($^{13}$C, at 193.85 ppm) and C-22 ($^{13}$C, at 128.76 ppm). In contrast, the β-H (21) showed correlations with both C-23 ($^{13}$C, at 123.97 ppm) and C-27 ($^{13}$C, at 106.53 ppm). On the other hand, the methyl group $CH_3$-6 ($^1$H, at 2.63 ppm) showed correlations with C-3 ($^{13}$C, at 143.36 ppm) and C-2 ($^{13}$C, at 114.20 ppm), whereas the H-11 signal ($^1$H, at 8.16 ppm) showed HMBC correlation with both C-1 ($^{13}$C, at 150.16 ppm) and C-9 ($^{13}$C, at 158.01 ppm).

The IR spectrum of the synthesized chalcone is presented in Fig. S3† and showed the presence of absorption bands at 3082, 2990 and 2894 cm$^{-1}$ due to aromatic and aliphatic C–H vibrations, the C=O, C=N and C=C stretching vibrations were identified as distinguishing absorption bands at 1655, 1589 and 1577 cm$^{-1}$ (see Table S2†).

The electrospray ionization-mass spectrometry (ESI-MS) of the title compound showed an $[M + H]^+$ peak of 398.1499, corresponding to the molecular formula $C_{24}H_{20}N_3O_3^+$. Thus, based on the above spectral data, the structure of the synthesized chalcone was confirmed (see Fig. S4†).

#### 4.1.1 Theoretical $^1$H and $^{13}$C NMR chemical shift analysis.

The $^1$H and $^{13}$C NMR chemical shifts of each atom within the title compound were studied both experimentally and theoretically. Chemical shift values were computed in chloroform at

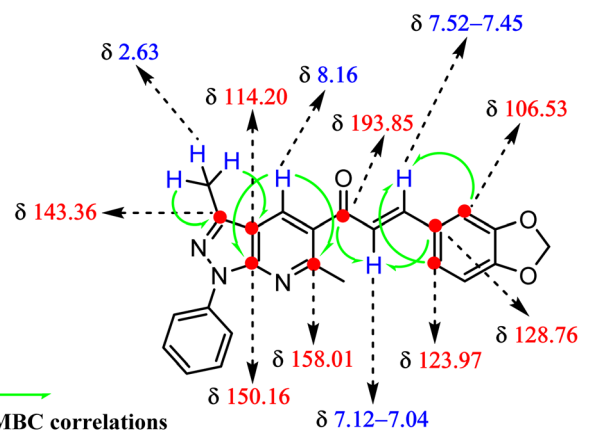


Fig. 1 HMBC-assisted NMR-based structural determination of compound **6**.

three different levels of theory (M062X, TPSS and B3LYP) using the Gauge-Independent Atomic Orbital (GIAO)[33] and 6-311++G(d,p) basis set and compared with the experimental NMR spectra in $CDCl_3$.

All computed and experimental $^1H$ and $^{13}C$ NMR chemical shift values are listed in Tables S3 and S4.† M062X and B3LYP systematically overestimated the chemical shift values in $^{13}C$, with high errors, greater than 20 ppm for some atoms. We have calculated the absolute errors in $^{13}C$ and found the following trend in the sum of the absolute errors: M062X > B3LYP > TPSS. In the case of the $^1H$ spectra, the next trend was found: M062X > B3LYP > TPSS.

Correlation graphs were prepared and given in Fig. S5 and S6.† A good linear correlation between experimental and theoretical $^1H$ and $^{13}C$ NMR chemical shift values of the title compound was observed as indicated by the $R^2$ values (see corresponding graphs in ESI†).

### 4.2 X-ray single crystal studies

The molecular structure of the title compound corresponds to a chalcone containing 2,2-dimethyl-1,3-benzodioxole and pyrazole[3,4-*b*]pyridine moieties. The piperonal chalcone shows a centrosymmetric setting with normal bond distances and angles.[51] The compound shows the *E* isomer in the solid state, being the most common conformation for this type of compound.[54,55] The ORTEP diagram of the title compound drawn at 30% probability thermal displacement ellipsoids with the atom numbering scheme is presented in Fig. 2. The molecule is essentially planar, which encourages us to study the NLO properties[54] of the title compound.

For the title compound, non-hydrogen atoms were refined with anisotropic displacement parameters. All hydrogen atoms were included in their calculated positions, assigned fixed isotropic thermal parameters, and constrained to ride on their parent atoms. The crystallographic data and the parameters of the refinement process of the title compound are given in Table 1.

In the crystal structure, one C–H···N intramolecular hydrogen bond interaction is observed with a graph-set motif[56] $S_1^1(6)$. Additionally, the molecules are linked by π–π interactions, observed between benzodioxole rings, and benzodioxole and pyridine rings with mean distance of 3.945 and 3.962 Å, distance plane-centroid of 1.602 and 1.872 Å, and angles between rings *α*, *β* and *γ* of 15.77(10)° and 0.02(11)°; 21.5° and 24.0°; 28.2° and 24.0°, respectively (see Fig. 3).

### 4.3 Comparison of geometry data

The root mean squared (RMS) value predicted by Chemcraft software, which accounts for the difference between the monomer from X-ray diffraction experiment and the

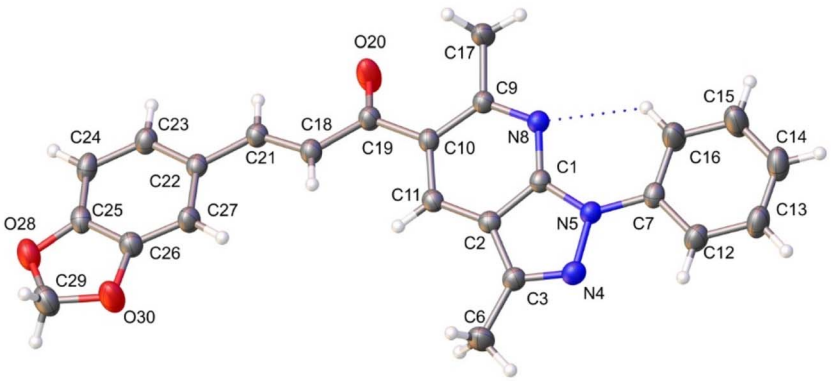


Fig. 2 ORTEP view of the title compound drawn at 30% of probability thermal displacement ellipsoids.

Table 1 Crystallographic data and refinement details for title compound **6**

| | | | |
|---|---|---|---|
| Empirical formula | $C_{24}H_{19}N_3O_3$ | Crystal size (mm) | 0.446 × 0.269 × 0.184 |
| Formula mass, g mol$^{-1}$ | 397.42 | *F*(000) | 416.0 |
| Collection *T*, K | 295.09 | Abs coeff. (mm$^{-1}$) | 0.090 |
| Crystal system | Triclinic | 2*θ* range (°) | 5.692 to 54.052 |
| Space group | $P\bar{1}$ | Range *h*, *k*, *l* | −11/10, −13/13, −13/14 |
| *a* (Å) | 8.669(6) | No. total refl. | 14 220 |
| *b* (Å) | 10.856(7) | No. unique refl. | 4213 [$R_{int}$ = 0.0373, $R_{sigma}$ = 0.0350] |
| *c* (Å) | 11.092(7) | Comp. $\theta_{max}$ (%) | 98.1 |
| *α* (°) | 95.470(16) | Max/min transmission | 0.984/0.971 |
| *β* (°) | 97.788(14) | Data/restraints/parameters | 4213/0/274 |
| *γ* (°) | 106.365(14) | Final *R* [$I > 2\sigma(I)$] | $R_1$ = 0.0521, w$R_2$ = 0.1209 |
| *V* (Å$^3$) | 982.5(11) | *R* indices (all data) | $R_1$ = 0.0926, w$R_2$ = 0.1544 |
| *Z* | 2 | Goodness of fit/$F^2$ | 1.021 |
| $\rho_{calcd}$ (g cm$^{-3}$) | 1.343 | Largest diff. peak/hole (e Å$^{-3}$) | 0.19/−0.19 |

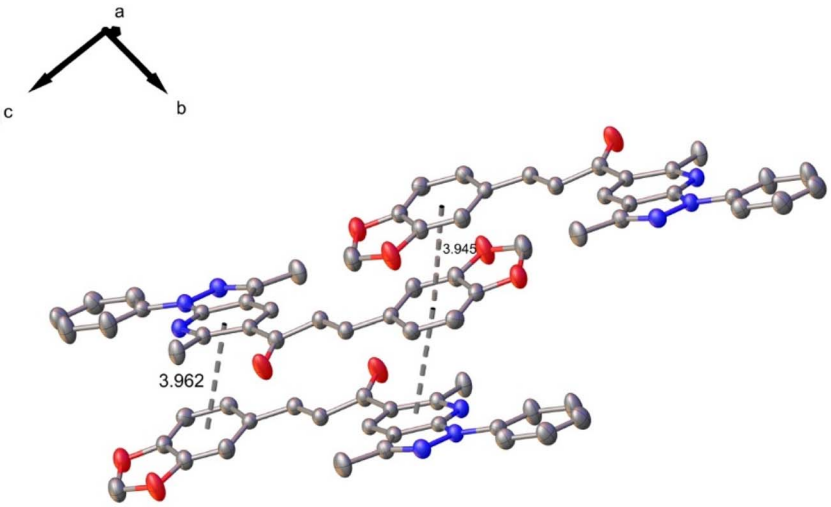


Fig. 3 $\pi-\pi$ interactions in compound **6**.

theoretically optimized geometry, was relatively low: 0.550 Å. Then, a good agreement was found between the optimized molecular geometrical parameters and experimental ones. Only a slight difference in the dihedral angle (C11, C10, C19 and C18) was shown between the monomer of X-ray diffraction experiment and the optimized geometry, which have values of 20.62 and 32.34, respectively. However, these results demonstrate the structural validity of the optimized geometry. A complete list of coordinates, bond lengths, bond angles and dihedral angles obtained by X-ray diffraction and DFT/M062X/6-311++G(d,p) of the title compound are presented in the ESI (see Tables S6–S8†).

### 4.4 UV-Vis studies and electronic properties

The comparison of the experimental and simulated theoretical UV-Vis spectra of piperonal chalcone has been studied. The experimental spectrum scanned in methanol solution within the range of 190–410 nm (Fig. 4a) includes two principal bands localized around 280 and 345 nm. These two bands were assigned to n $\rightarrow$ $\pi^*$ and $\pi \rightarrow \pi^*$ electronic transitions. The theoretical electronic spectrum (Fig. 4b) shows two principal $\pi \rightarrow \pi^*$ electronic transitions located around 334 and 329 nm near the experimental signal. On the other hand, the theoretical electronic spectrum presents two local maximums with oscillator strengths (*f*) of 0.2993 and 0.2574, which are localized around 282 and 255 nm, respectively, and agree with the experimental UV-Vis spectra. As can also be seen in Fig. 4, the theoretical spectrum presents only values higher than 219 nm. Those values lower than this wavelength could not be simulated in our TDDFT calculations. Overall, the theoretical UV-Vis spectrum shows that the absorption values are at the exact location of the experimental average (*x*-axis in Fig. 4). However, the calculated absorbance value does not match the experimental value because this measurement is directly proportional to the sample concentration, which cannot be calculated in our Gaussian experiment. To obtain absorbance values close to the experimental ones, it is necessary to model different geometrical conformations using explicit solution methods involving a long computational process, which is an unintended goal of this work.

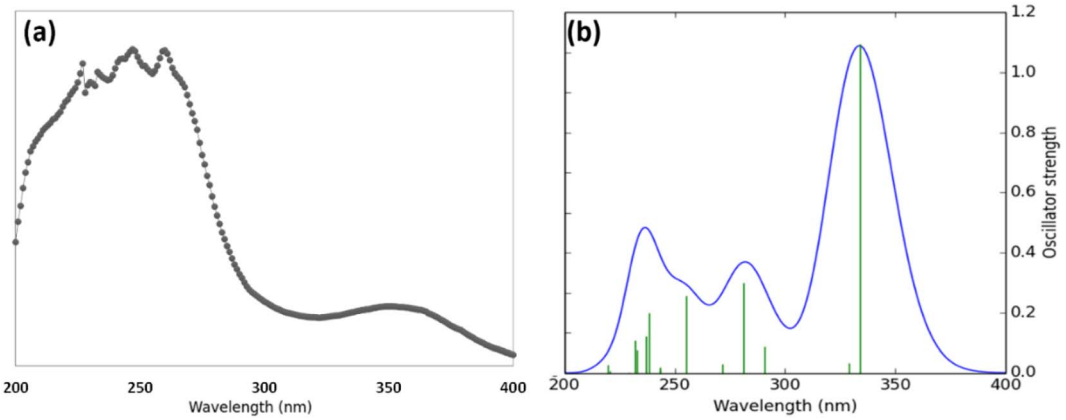


Fig. 4 Experimental (a) and calculated (b) electronic absorption spectra of title compound.

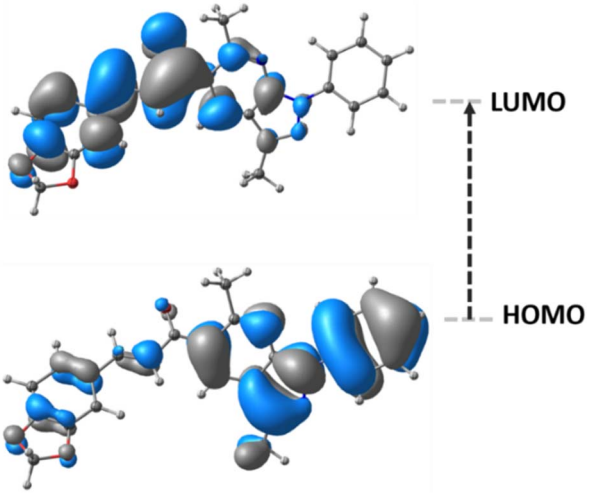


Fig. 5 Frontier molecular orbitals of title compound.

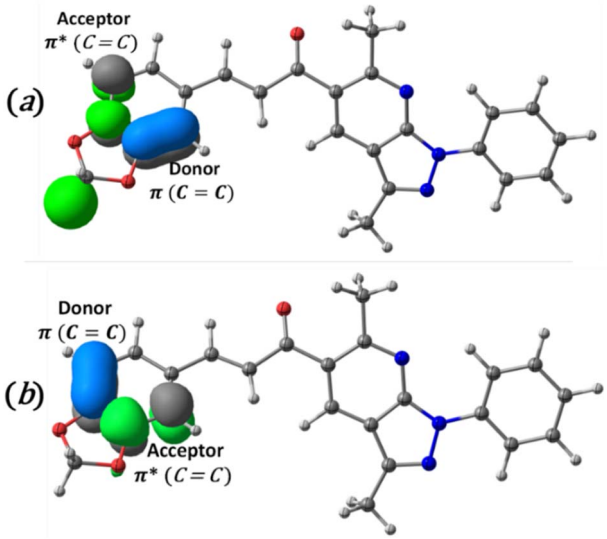


Fig. 6 Schematic diagram of intramolecular charge transfer from C=C π bond to C=C π antibonding and the second-order perturbation energies ($E^{(2)}$). (a) 1138.4 kcal mol$^{-1}$ and (b), 161.2 kcal mol$^{-1}$.

### 4.5 Frontier molecular orbitals (FMOs) analysis and molecular reactivity

The frontier molecular orbitals (FMOs), HOMO and LUMO, are the main orbitals responsible for chemical stability or reactivity. The HOMO–LUMO plots for the title compound is shown in Fig. 5. The molecular form of HOMO shows a high electron density located over N–C groups. In the case of LUMO, the highest probability regions are in the same area as the HOMO, thus an allowed electronic transition could occur between these two states.

HOMO energy is associated with the electron-donating ability of a compound, whereas LUMO energy with electron-accepting. The frontier molecular orbital energy gap provides information about the chemical reactivity and kinetic stability. A molecule with a small frontier orbital gap is associated with a high chemical reactivity and low kinetic stability.

The HOMO and LUMO energies, and frontier orbital energy gap of the title compound were found to be 7.2861, −1.5934, and 5.6926 eV, respectively. The calculated values of the chemical hardness, chemical potential, electrophilicity index, and chemical softness parameters for the compound described above are 2.84, −4.43, 3.46 eV, and 0.17 eV$^{-1}$, respectively.

The piperonal chalcone derivative is expected to be less polarizable and associated with a low chemical reactivity due to its larger molecular gap and chemical hardness values, indicating a hard molecule with low polarizability with high kinetic stability.

### 4.6 Natural bond orbital (NBO) analysis

The charge transfer and intramolecular interactions between the occupied and unoccupied molecular orbitals of the title compound were analyzed through the natural bond orbital (NBO) analysis. The analysis of second-order perturbation energy[57] ($E^{(2)}$) showed that the two most important donor–acceptor intermolecular interactions (Fig. 6) presented in the compound are interactions between C=C π and C=C π antibonding orbitals, with energies values of 1138.4 (Fig. 6a) and 161.2 (Fig. 6b) kcal mol$^{-1}$, respectively. This mixing of donors and acceptors leads to an overall decrease in stabilization energy.

### 4.7 Nonlinear optical (NLO) properties

The dipole moment, polarizability and hyperpolarizability results are presented in Table 2. Urea has been used as a prototype molecule for a comparative approach to NLO properties.[58]

The relevance of polarizability and hyperpolarizability of a molecular system depends on electronic communication between two different parts of a molecule. The results showed non-zero $\mu$ values for the title compound, which should cause microscopic quadratic and cubic hyperpolarizabilities, with resulting non-zero values derived by the second numerical derivatives of electric dipole moments to the field implemented (see Table 2). The calculated dipole moment ($\mu$) for the title compound is 1.29 times higher than that obtained from urea. The non-zero $\langle\alpha\rangle$, $\langle\beta\rangle$ and $\langle\gamma\rangle$ tensors values for the title compound predict the ability to acquire second- and third-order microscopic NLO responses. The of $\alpha$, $\beta$ and $\gamma$ calculated values for the title compound are 10.5, 66.3 and 46.7 times higher than those obtained from urea. Since we lack experimental data on NLO properties, the implemented theoretical analyses provide a predictive tool to show that the studied compound can be usefully applied in this field. To be more confident of these results, we have added the same theoretical analysis for two reported molecules with optical properties and structures similar to our studied compound (Table 2). Surprisingly the $\alpha$, $\beta$ and $\gamma$ calculated values of our compound present better results than reference molecules. Hence, compared with urea and the other two molecules with NLO properties, the title compound may fulfill many of the quadratic optical

Table 2 Dipole moment, polarizability and hyperpolarizability values at CAM-B3LYP/6-311++g(d,p) level

| | $\mu$ (D) | $\alpha$ ($\times 10^{-24}$ esu) | $\beta$ ($\times 10^{-30}$ esu) | $\gamma$ ($\times 10^{-36}$ esu) |
|---|---|---|---|---|
| Urea | 3.875 | 4.823 | 0.414 | 2.941 |
| Studied compound (**6**) | 5.007 | 50.830 | 27.464 | 137.399 |
| (*E*)-1-(1,3-Benzodioxol-5-yl)-4,4-dimethylpent-1-en-3-one[59] | 3.546 | 27.625 | 22.413 | 44.189 |
| (2*E*)-1-(1,3-Benzodioxol-5-yl)-3-phenylprop-2-en-1-one (SSP1)[60] | 3.011 | 31.346 | 8.344 | 67.879 |

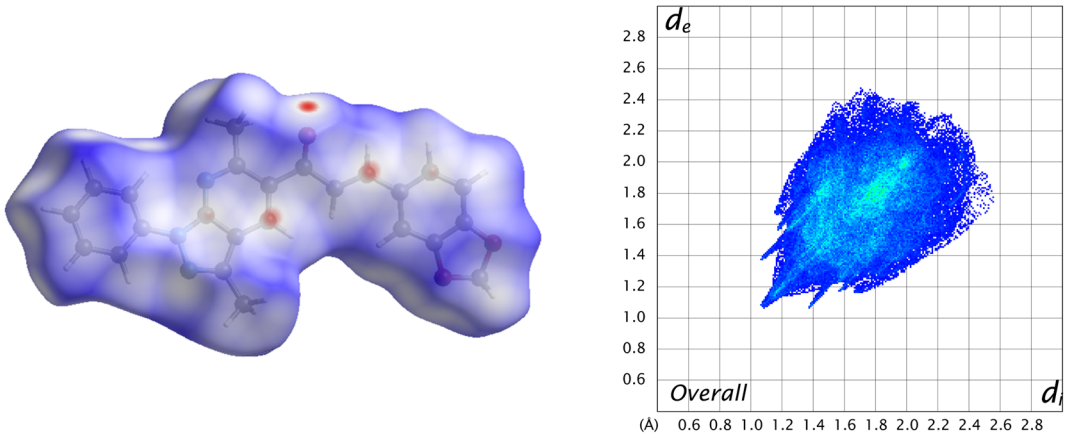


Fig. 7 Overall Hirshfeld surface (left) and its fingerprint plot (right).

nonlinearity requirements and could have potential applications in NLO and electro-optic devices.

### 4.8 Hirshfeld surface analysis and 2D fingerprint plots

Visualization of intermolecular contacts through the crystal structure was achieved by Hirshfeld surface analysis and was performed as a complement to XRD analysis. The $d_{norm}$ surfaces were visualized with three colors, white indicates the contacts with distances equal to the sum of the van der Waals radii ($d_{norm}$ = VdW radii), blue areas show the positive electrostatic potential (hydrogen-bond donors, $d_{norm}$ > VdW radius), and red regions indicate the negative electrostatic potential (hydrogen-bond acceptors, $d_{norm}$ < VdW radii).[50] All the contacts contributing to the total area of the surface are illustrated in Fig. 7.

A 48.2% contribution with pair of sharp needles and the tip at $d_i + d_e \approx 2.2$ Å was noticed from H···H contacts, covering a significant region of the entire Hirshfeld surface. These interactions generate an important effect on the molecular packing in the intermolecular stabilization. These short H···H contact links adjacent molecules into inversion related generating dimers (Fig. 8). The second important interaction is C–H···C, contributing 18.8% to the overall crystal packing. Moreover, C–H···O and C–H···N bond interactions have contributions of 15% each.

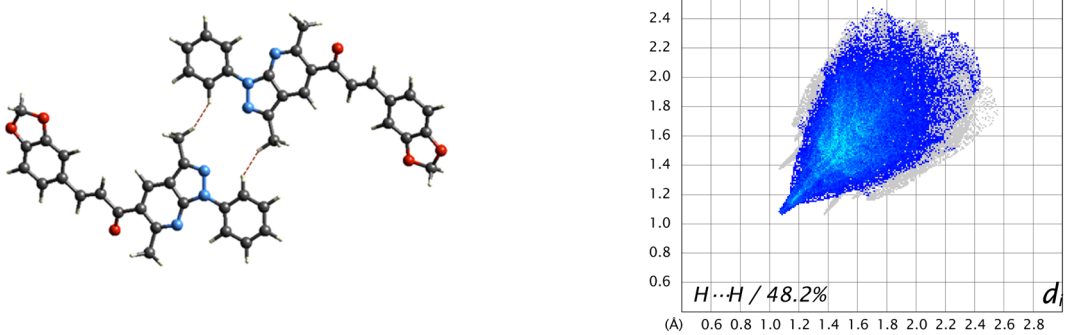


Fig. 8 Short H···H contact interactions in the crystal structure stabilization of the title compound.

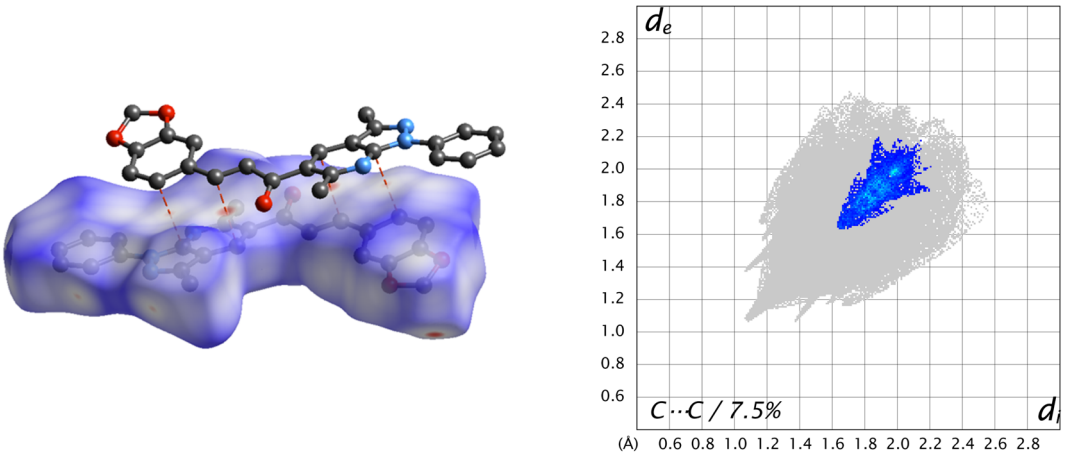


Fig. 9 $d_{norm}$ surface of the title compound (left) and its fingerprint plot (right), showing π···π stacking interactions in the title compound.

Another type of weak C···C contact gives only 7.5% of the surface with the tip at $d_e + d_i \approx 3.4$ Å, which helps in understanding interactions π···π stacking (Fig. 9).

### 4.9 Energy frameworks

The energy framework[61] was performed to obtain the intermolecular interaction energies. This method allows analysis and visualization of the three-dimensional crystal packing to analyze the three-dimensional crystal topology. The interaction energy is calculated and compared using the formula $E_{tot} = E_{ele} + E_{pol} + E_{dis} + E_{rep}$ (where $E_{ele}$ is the electrostatic component, $E_{pol}$ the polarization energy, $E_{dis}$ the dispersion energy, and $E_{rep}$ the exchange repulsion energy) based on the anisotropy of the topology of pairwise intermolecular interaction energies. The thickness of the cylinder radius indicates the grade of interaction energies.[62]

According to the tube direction, it can be concluded that the formation of the framework is directed by the translational or centrosymmetric elements. However, this rearrangement allows the formation of other weak interactions in the crystal structure. The energy framework is presented in Fig. 10. The dispersion ($E_{dis}$) energy shows a zig-zag rod shape energy topologies along *c*-axis, as a component of the framework energy being less dominating than $E_{ele}$. In this case, the rearrangement is reinforced by the presence of weak interactions in the crystal structure, such as π···π and classic hydrogen bond interactions, but not enough for the better stabilization of the framework.

The total interaction energies are electrostatics ($E_{ele}$ = −40.1 kJ mol$^{-1}$), polarization ($E_{pol}$ = −7.7 kJ mol$^{-1}$), dispersion ($E_{dis}$ = −210.2 kJ mol$^{-1}$), repulsion ($E_{rep}$ = 104.7 kJ mol$^{-1}$), and total interaction energy ($E_{tot}$ = −153.3 kJ mol$^{-1}$). The sum of dispersion energies (−210.2 kJ mol$^{-1}$) is greater than that of electrostatic energies (−40.1 kJ mol$^{-1}$) for the title compound and this low value is attributed to the absence or few numbers of classical hydrogen bonds (see Table 3). According to the result obtained, the

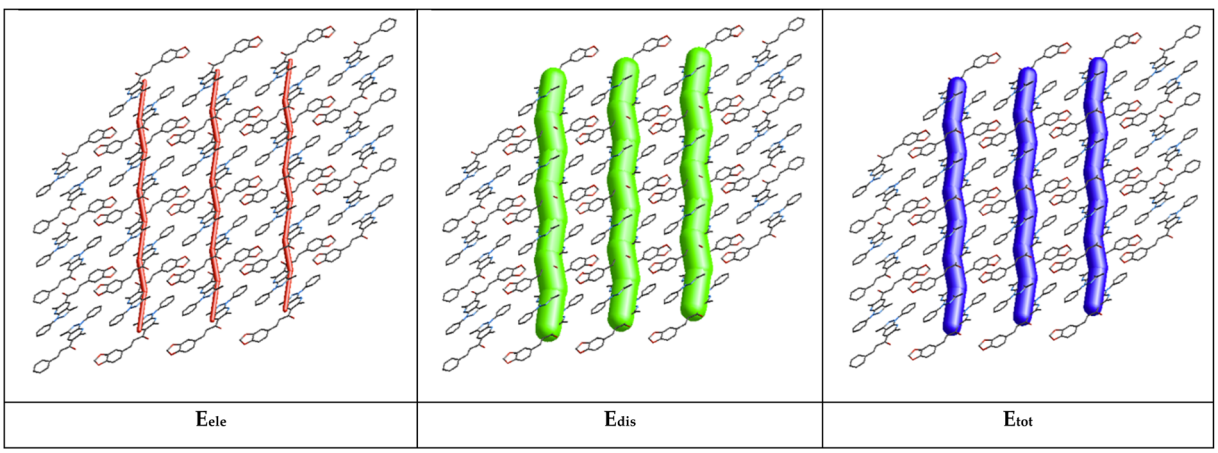


Fig. 10 Energy framework diagram for electrostatic ($E_{ele}$, red), (b) dispersion ($E_{dis}$, green), and (c) total interaction energy ($E_{tot}$, blue) of the title molecule.

Table 3 Total energy force diagrams and interaction details with symmetry operation (Symop) and distances between molecular centroids ($R$) in Å for compounds

| No. | Symop | $R$ | $E_{ele}$ | $E_{pol}$ | $E_{dis}$ | $E_{rep}$ | $E_{tot}$ |
|---|---|---|---|---|---|---|---|
| 1 | $-x, -y, -z$ | 4.43 | −23 | −3.3 | −107 | 56.3 | −77 |
| 1 | $x, y, z$ | 10.9 | 1.4 | −0.2 | −3.2 | 0 | −2.0 |
| 1 | $-x, -y, -z$ | 6.71 | −18.5 | −4.2 | −100 | 48.4 | −74.3 |
| Total energies | | | −40.1 | −7.7 | −210.2 | 104.7 | −153.3 |

dispersion energy framework has a significant contribution over the electrostatic energy framework.

## 5 Conclusions

In this work, we have presented the data and results used in confirming the structural properties of a π-conjugate system combining the chalcone and the pyrazole[3,4-*b*]pyridine scaffolds. The chalcone crystal has been synthesized and fully characterized by UV-Visible, FT-IR, HRMS, $^{1}$H NMR, and $^{13}$C NMR spectroscopic studies and X-ray crystallography. The X-ray findings showed that the studied molecule has planar molecular geometry and crystallizes in the triclinic system with a $P\bar{1}$ space group, $Z = 2$, and unit cell parameters $a = 8.669(6)$ Å; $b = 10.856(7)$ Å, $c = 11.092(7)$ Å, $\beta = 97.788(14)°$ and $V = 982.5(11)$ Å$^3$. In general, good agreement was found between all the theoretical properties investigated (structural, electronic, and spectroscopic) and the experimental ones. Molecular stability from hyper conjugative interactions and charge delocalization was analyzed using NBO analysis. The FMOs analysis and chemical reactivity descriptors revealed that the piperonal chalcone is a less reactive and more stable molecule. Hirshfeld surface analysis of the crystal structure indicated that the largest contribution to the intermolecular stabilization in the crystal packing comes from the H···H (48.2%) bond interactions. Furthermore, the calculated interaction energy suggested that the dispersion energy framework significantly contributes to the total energy framework. According to the computed $\alpha$, $\beta$, and $\gamma$ values, the chalcone crystal exhibits significant NLO properties. Thus, we concluded that the piperonal chalcone is a promising candidate for future applications in nonlinear optical devices.

## Conflicts of interest

There are no conflicts to declare.

## Acknowledgements

A FONDECYT project number 1200531 supported this research. The authors also acknowledge to FONDEQUIP program (EQM 130021, 180024 and 170172). E. P.-C. thanks FONDECYT Post-Doctoral Fellowship No. 3220681. "Powered@NLHPC: This research/thesis was partially supported by the supercomputing infrastructure of the NLHPC (ECM-02)".

## References

1 S. Basu, *Ind. Eng. Chem. Prod. Res. Dev.*, 1984, **23**, 183–186.
2 A. Abudurusuli, J. Li and S. Pan, *Dalton Trans.*, 2021, **50**, 3155–3160.
3 S. Tao, T. Miyagoe, A. Maeda, H. Matsuzaki, H. Ohtsu, M. Hasegawa, S. Takaishi, M. Yamashita and H. Okamoto, *Adv. Mater.*, 2007, **19**, 2707–2710.
4 I. D. Borges, J. A. V. Danielli, V. E. G. Silva, L. O. Sallum, J. E. Queiroz, L. D. Dias, I. Iermak, G. L. B. Aquino, A. J. Camargo, C. Valverde, C. Valverde, F. A. P. Osório, F. A. P. Osório, B. Baseia, B. Baseia, H. B. Napolitano and H. B. Napolitano, *RSC Adv.*, 2020, **10**, 22542–22555.
5 S. Raghavendra, K. V. Anil Kumar, T. Chandra Shekhara Shetty and S. M. Dharmaprakash, *J. Mol. Struct.*, 2014, **1074**, 653–659.
6 I. Polyzos, G. Tsigaridas, M. Fakis, V. Giannetas, P. Persephonis and J. Mikroyannidis, *Chem. Phys. Lett.*, 2003, **369**, 264–268.
7 R. L. Sutherland, D. G. Mclean and S. Kirkpatrick, *Handbook of Nonlinear Optics*, 2nd edn, Revised and Expanded, 2003.
8 K. Naseema, V. Rao, K. B. Manjunatha, G. Umesh, K. V. Sujith and B. Kalluraya, *J. Opt.*, 2010, **39**, 143–148.
9 M. Makowska-Janusik, E. Gondek, I. V. Kityk, J. Wisła, J. Sanetra and A. Danel, *Chem. Phys.*, 2004, **306**, 265–271.
10 J. Chen, Q. Ren, X. Wang, T. Li, H. Yang, J. Zhang and G. Li, *Opt.*, 2012, **123**, 1761–1764.
11 J. P. Abraham, D. Sajan, V. Shettigar, S. M. Dharmaprakash, I. Němec, I. Hubert Joe and V. S. Jayakumar, *J. Mol. Struct.*, 2009, **917**, 27–36.
12 K. Ozga, E. Gondek, A. Danel and K. Chaczatrian, *Opt. Commun.*, 2004, **231**, 437–446.
13 L. Shen, Z. Li, X. Wu, W. Zhou, J. Yang and Y. Song, *RSC Adv.*, 2020, **10**, 15199–15205.
14 E. D. Dsilva, D. Narayan Rao, R. Philip, R. J. Butcher, Rajnikant and S. M. Dharmaprakash, *J. Phys. Chem. Solids*, 2011, **72**, 824–830.
15 S. R. Marder, W. E. Torruellas, M. Blanchard-Desce, V. Ricci, G. I. Stegeman, S. Gilmour, J. L. Brédas, J. Li, G. U. Bublitz and S. G. Boxer, *Science*, 1997, **276**, 1233–1236.
16 V. Shettigar, P. S. Patil, S. Naveen, S. M. Dharmaprakash, M. A. Sridhar and J. Shashidhara Prasad, *J. Cryst. Growth*, 2006, **295**, 44–49.
17 B. Gu, W. Ji, X.-Q. Huang, P. S. Patil and S. M. Dharmaprakash, *Opt. Express*, 2009, **17**, 1126.
18 H. J. Ravindra, A. J. Kiran, S. M. Dharmaprakash, N. Satheesh Rai, K. Chandrasekharan, B. Kalluraya and F. Rotermund, *J. Cryst. Growth*, 2008, **310**, 4169–4176.
19 P. Poornesh, K. Ravi, G. Umesh, P. K. Hegde, M. G. Manjunatha, K. B. Manjunatha and A. V. Adhikari, *Opt. Commun.*, 2010, **283**, 1519–1527.
20 B. Gu, W. Ji, P. S. Patil, S. M. Dharmaprakash and H. T. Wang, *Appl. Phys. Lett.*, 2008, **92**, 091118.

21 S. Y. Priya, R. K. Rao, V. P. Chalapathi and C. Author, *J. Clin. Med. Images Short Reports*, 2018, **1**, 1–9.
22 R. Kumar, T. Karthick, P. Tandon, P. Agarwal, A. P. Menezes and A. Jayarama, *J. Mol. Struct.*, 2018, **1164**, 180–190.
23 A. P. Menezes and A. Jayarama, *J. Mol. Struct.*, 2014, **1075**, 246–253.
24 A. J. Kiran, H. W. Lee, H. J. Ravindra, S. M. Dharmaprakash, K. Kim, H. Lim and F. Rotermund, *Curr. Appl. Phys.*, 2010, **10**, 1290–1296.
25 E. Polo, K. Ferrer-Pertuz, J. Trilleras, J. Quiroga and M. Gutiérrez, *RSC Adv.*, 2017, **7**, 50044–50055.
26 Bruker, *APEX3, SAINT and SADABS*, Bruker AXS Inc., Madison, Wisconsin, USA, 2016.
27 G. M. Sheldrick, *Acta Crystallogr., Sect. C: Struct. Chem.*, 2015, **71**, 3–8.
28 O. V Dolomanov, L. J. Bourhis, R. J. Gildea, J. A. K. Howard and H. Puschmann, *J. Appl. Crystallogr.*, 2009, **42**, 339–341.
29 R. Krishnan, J. S. Binkley, R. Seeger and J. A. Pople, *J. Chem. Phys.*, 1980, **72**, 650–654.
30 A. D. McLean and G. S. Chandler, *J. Chem. Phys.*, 1980, **72**, 5639–5648.
31 Y. Zhao and D. G. Truhlar, *Theor. Chem. Acc.*, 2008, **120**, 215–241.
32 M. J. Frisch, G. Trucks, H. Schlegel, G. Scuseria, M. Robb, J. Cheeseman, J. Montgomery, T. Vreven, K. Kudin, J. Burant, J. Millam, S. Iyengar, J. Tomasi, V. Barone, B. Mennucci, M. Cossi, G. Scalmani, N. Rega, G. Petersson, H. Nakatsuji, M. Hada, M. Ehara, K. Toyota, R. Fukuda, J. Hasegawa, M. Ishida, T. Nakajima, Y. Honda, O. Kitao, H. Nakai, M. Klene, X. Li, J. Knox, H. Hratchian, J. Cross, V. Bakken, C. Adamo, J. Jaramillo, R. Gomperts, R. Stratmann, O. Yazyev, A. Austin, R. Cammi, C. Pomelli, J. Ochterski, P. Ayala, K. Morokuma, G. Voth, P. Salvador, J. Dannenberg, V. Zakrzewski, S. Dapprich, A. Daniels, M. Strain, O. Farkas, D. Malick, A. Rabuck, K. Raghavachari, J. Foresman, J. Ortiz, Q. Cui, A. Baboul, S. Clifford, J. Cioslowski, B. Stefanov, G. Liu, A. Liashenko, P. Piskorz, I. Komaromi, R. Martin, D. Fox, T. Keith, A. Laham, C. Peng, A. Nanayakkara, M. Challacombe, P. Gill, B. Johnson, W. Chen, M. Wong, C. Gonzalez, D. J. Fox and J. Pople, *Gaussian 09, Revision A.08*, Gaussian, Inc., 2009.
33 K. Wolinski, J. F. Hinton and P. Pulay, *J. Am. Chem. Soc.*, 1990, **112**, 8251–8260.
34 V. Barone and M. Cossi, *J. Phys. Chem. A*, 1998, **102**, 1995–2001.
35 M. Cossi, N. Rega, G. Scalmani and V. Barone, *J. Comput. Chem.*, 2003, **24**, 669–681.
36 A. Klamt and G. Schüürmann, *J. Chem. Soc., Perkin Trans. 2*, 1993, 799–805.
37 J. Andzelm, C. Kölmel and A. Klamt, *J. Chem. Phys.*, 1995, **103**, 9312–9320.
38 R. Bauernschmitt and R. Ahlrichs, *Chem. Phys. Lett.*, 1996, **256**, 454–464.
39 M. E. Casida, C. Jamorski, K. C. Casida and D. R. Salahub, *J. Chem. Phys.*, 1998, **108**, 4439–4449.
40 S. Miertuš, E. Scrocco and J. Tomasi, *Chem. Phys.*, 1981, **55**, 117–129.
41 J. L. Pascual-ahuir, E. Silla and I. Tuñon, *J. Comput. Chem.*, 1994, **15**, 1127–1138.
42 H. Chermette, *J. Comput. Chem.*, 1999, **20**, 129–154.
43 F. W. E. D. Glendening, J. K. Badenhoop, A. E. Reed, J. E. Carpenter, J. A. Bohmann, C. M. Morales, 2013.
44 Y.-Y. Hu, S.-L. Sun, S. Muhammad, H.-L. Xu and Z.-M. Su, *J. Phys. Chem. C*, 2010, **114**, 19792–19798.
45 H.-B. Zhao, Y.-Q. Qiu, C.-G. Liu, S.-L. Sun, Y. Liu and R.-S. Wang, *J. Organomet. Chem.*, 2010, **695**, 2251–2257.
46 M. A. Spackman and J. J. McKinnon, *CrystEngComm*, 2002, **4**, 378–392.
47 M. J. Turner, J. J. McKinnon, S. K. Wolff, D. J. Gromwood, P. R. Spackman, D. J. - Alitaka and M. A. Spackman, *Crystal Explorer*, University of Western Australia, 2017.
48 S. S. Batsanov, *Inorg. Mater. Transl. from Neorg. Mater. Orig. Russ. Text*, 2001, **37**, 871–885.
49 A. Bondi, *J. Phys. Chem.*, 1964, **68**, 441–451.
50 M. A. Spackman, J. J. McKinnon and D. Jayatilaka, *CrystEngComm*, 2008, **10**, 377–388.
51 F. H. Allen, O. Kennard, D. G. Watson, L. Brammer, A. G. Orpen and R. Taylor, *J. Chem. Soc., Perkin Trans. 2*, 1987, S1–S19.
52 J. Tirado-Rives and W. L. Jorgensen, *J. Chem. Theory Comput.*, 2008, **4**, 297–306.
53 A. D. Becke, *J. Chem. Phys.*, 1993, **98**, 5648–5652.
54 D. A. Zainuri, M. Abdullah, S. Arshad, M. S. A. Aziz, G. Krishnan, H. Bakhtiar and I. A. Razak, *Opt. Mater.*, 2018, **86**, 32–45.
55 B. Evranos Aksöz and R. Ertan, *FABAD J. Pharm. Sci.*, 2011, **36**, 223–242.
56 J. Bernstein, R. E. Davis, L. Shimoni and N. -L Chang, *Angew. Chem., Int. Ed. Engl.*, 1995, **34**, 1555–1573.
57 A. E. Reed and F. Weinhold, *J. Chem. Phys.*, 1985, **83**, 1736–1740.
58 C. Cassidy, J. M. Halbout, W. Donaldson and C. L. Tang, *Opt. Commun.*, 1979, **29**, 243–246.
59 R. I. Al-Wabli, K. S. Resmi, Y. Sheena Mary, C. Yohannan Panicker, M. I. Attia, A. A. El-Emam and C. Van Alsenoy, *J. Mol. Struct.*, 2016, **1123**, 375–383.
60 S. Shettigar, P. Poornesh, G. Umesh, B. K. Sarojini, B. Narayana and K. Prakash Kamath, *Opt. Laser Technol.*, 2010, **42**, 1162–1166.
61 C. F. Mackenzie, P. R. Spackman, D. Jayatilaka and M. A. Spackman, *IUCrJ*, 2017, **4**, 575–587.
62 H. A. Khamees, K. Chaluvaiah, N. A. El-khatatneh, A. Swamynayaka, K. H. Chong, J. P. Dasappa and M. Madegowda, *Acta Crystallogr., Sect. E: Crystallogr. Commun.*, 2019, **75**, 1620–1626.